https://doi.org/10.1016/j.jmapro.2023.03.017

Enhancement on mechanical properties of CoCrNi medium entropy alloy via cold spray additive manufacturing associated with sintering

Yongyun Zhang [a, b], Bailiang Qin[a], KangCheung Chan [a*], Rocco Lupoi[b], Shuo Yin[b*], Yingchun Xie[c], Shulong Ye[d], Peng Yu[e], Haibo Ke[f], Weihua Wang[f,g]

a. State Key Laboratory of Ultra-precision Machining Technology, Department of Industrial and Systems Engineering, The Hong Kong Polytechnic University, Hong Kong, China

b. Trinity College Dublin, the University of Dublin, Department of Mechanical and Manufacturing Engineering, Parsons Building, Dublin 2, Ireland

c. National Engineering Laboratory for Modern Materials Surface Engineering Technology, The Key Lab of Guangdong for Modern Surface Engineering Technology, Guangdong Institute of New Materials, Guangzhou, 510651, PR China

d. Faculty of Materials Science, Shenzhen MSU-BIT University, Shenzhen 518172, China

d. Department of Materials Science and Engineering, Southern University of Science and Technology, Shenzhen 518055, China

e. Songshan Lake Materials Laboratory, Dongguan 523808, China

f. Institute of Physics, Chinese Academy of Sciences, Beijing 100190, China

□Corresponding author.
E-mail address: kc.chan@polyu.edu.hk

□Corresponding author.
E-mail address: yins@tcd.ie

Abstract

Equimolar CoCrNi medium entropy alloy (MEA) has a broad potential for industrial applications due to its excellent strength-ductility synergy. In this study, the emerging solid-state cold spray additive manufacturing (CSAM) approach was applied to fabricate bulk CoCrNi MEA deposits for the first time. However, due to its nature, CSAM normally results in limited metallurgical bonding and weak interfacial bonding between deformed particles, particularly for high-strength alloys such as the CoCrNi MEA used in this work. Therefore, a post-sintering treatment with temperatures ranging from 1200 °C to 1350 °C was applied after CSAM to improve the interparticle bonding and strengthen the as-fabricated MEA deposits. During the sintering process, recovery, recrystallization, sintering necks and grain migration for polycrystalline growth were observed at different stages. The sintering treatment significantly enhanced the tensile strength and ductility of the as-fabricated sample from ~240 MPa and ~2% to ~660 MPa and 43%. This study validates the potential of the united CSAM-sintering strategy in additive manufacturing of CoCrNi MEA.

Key words: CoCrNi medium entropy alloy; cold spraying additive manufacturing; sintering strategies; microstructures evolution; properties improvement

1. Introduction

Different from traditional alloys, high entropy alloys (HEAs) are constructed with five or more principal alloying elements in equimolar or near-equimolar ratios, and have no main component [1]. They are novel materials with superior properties such as good ductility-strength synergy, excellent damping properties, wear, corrosion and oxidation resistance [2–6], which of importance to engineering materials Based on similar material designing philosophy, medium entropy alloys (MEAs), represented by equimolar CoCrNi alloy, have been developed in recent years. Such kinds of MEAs exhibit comparable or even superior properties to the CoCrFeNiMn HEA [7–9].

The traditional method for the fabrication of bulk CoCrNi MEA is casting. However, post-machining is necessary for shaping the cast MEA into final components for industrial applications. Conventional subtractive machining process results in massive material waste, and is difficult to fabricate components with complex structures. In contrast, additive manufacturing technologies can fabricate MEA components directly into near-net-shape with little to no post-machining effort. Cold spray additive manufacturing (CSAM) is an emerging solid-state additive manufacturing process [10–12]. During CSAM, powders are accelerated to a high speed in a De-Laval nozzle, and sprayed onto a substrate [13,14]. Upon impact, significant plastic deformation occurs in these powders, resulting in temperature rise at localized contact region and leading to metallurgical bonding at interparticle interfaces. As such, powders are deposited layer by layer and eventually consolidate into a near-net-shape

component. CSAM can fabricate free-standing metal components and also restore damaged metal components with little post-machining work [10,11,15]. As compared to fusion-based additive manufacturing technologies, such as selective laser melting and laser metal deposition, one of the major attractive advantages of CSAM is the ability for fabricating components made of high-reflectivity metals (e.g., Cu and Al), which are considered difficult to manufacture using laser-based additive manufacturing processes [16]. Short production time, large product size, high efficiency, low thermal effect, and higher flexibility also render CSAM a promising additive manufacturing process.

However, the major drawback of CSAM is the unfavorable mechanical properties of the deposits in their as-fabricated state, particularly when using high-strength alloy powders such as stainless steel [17], Ti alloys [18] and HEAs [4,6]. Higher gas pressure or temperature or using helium as propulsive gas can improve the strength and ductility of the deposits to some extent, however, such improvement is insufficient to result in high-performance CSAM components from the perspective of practical industrial applications. Therefore, post-treatment for improving the mechanical properties of CSAM deposits is vital. Some post-treatment processes such as hot-rolling [16,19–22], friction stir processing [23] and hot isostatic pressing [18,24] can improve the mechanical performance of CSAM deposits, but their complicated and/or costly procedures limit their wide applications. Annealing is the simplest and the most economical method for improving the microstructure and mechanical properties of

CSAM deposits [17,19,20,25–31]. The improvement is achieved through recrystallization and complete metallurgical bonding within deformed particles and across adjacent particles [17]. However, the applied annealing temperatures are typically too low to induce strong interparticle metallurgical connections, and thus the improvement of the properties of CSAM deposits is limited [17,25,30]. It is known that sintering occurs when the heat-treated temperatures are higher than 70% of the melting temperature (T_m/K) [32]. The sintering necks that are formed during sintering process can result in a much stronger metallurgical bonding between adjacent powders as compared to conventional annealing [17,25,30]. Therefore, sintering could be another potential heat treatment method for CSAM deposits.

In our study, CSAM was applied for the first time to deposit CoCrNi MEA. Since CoCrNi is a high-strength alloy, its CSAM deposit may possess unfavorable mechanical properties in the as-fabricated state. Therefore, sintering was used as a post-treatment method to strengthen the as-fabricated deposits. Different sintering strategies were used to reveal their influence on the microstructure evolution and mechanical properties of CSAM CoCrNi deposit.

2. Experimental procedure

2.1 Powder materials

Pre-alloyed equimolar CoCrNi powder (Vilory Ltd. China) was used as the feedstock. The median size of the powders was measured as 13.6 μm by a laser particle size analyzer (Mastersizer 3000), shown in Fig. 1. Fig. 2 shows the morphology of

powders used in our study, characterized by scanning electron microscopy (SEM, Merlin, Zeiss) equipped with electron backscattering diffraction (EBSD, Digview 4, EDAX). From Fig. 2 (a), it is seen that the pre-alloyed CoCrNi powders have a spherical shape with a uniform size distribution. The results of EBSD and energy disperse spectroscopy (EDS, Octane Pro, EDAX) reveals that the equiaxed grains with an evenly distributed alloying element were produced after the gas atomization process. The chemical composition of the powders was measured as 34.72 at.% for Co, 32.53 at.% for Cr, and 32.75 at.% for Ni by EDS.

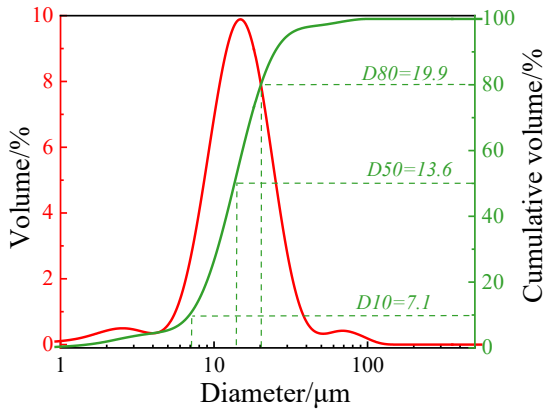

Fig. 1 CoCrNi MEA powder size distribution

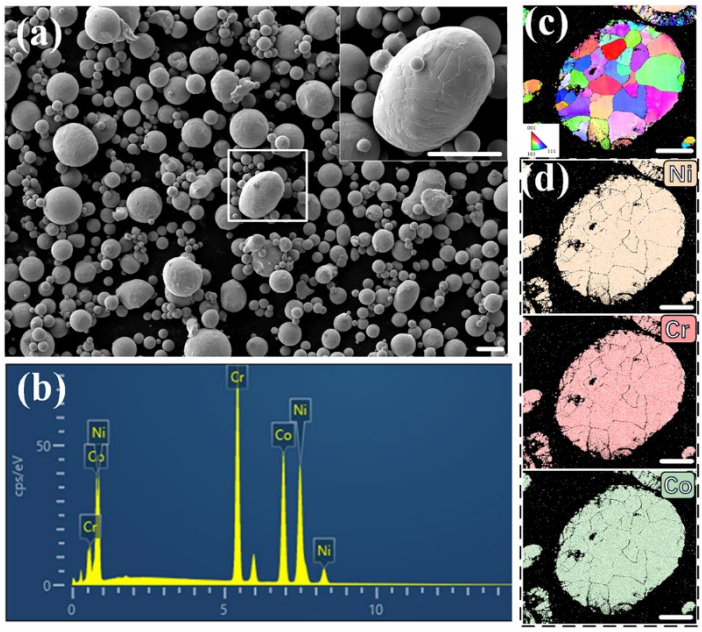

Fig. 2 CoCrNi MEA powders: (a) morphology in SEM with (b) corresponding EDS spectrums; (c) inverse pole figure (IPF) map with (d) corresponding elements EDS maps (scale bar is 10 μm)

2.2 Cold spray procedure

The powders were sprayed onto a 5mm thick 6082 Al alloy substrate via a commercial cold spray system (Plasma Giken, Japan), using compressed nitrogen as the propulsion gas. The inlet pressure and temperature of the nitrogen were 5.0 MPa and 1000 °C, respectively. The standoff distance between the substrate and nozzle was 30 mm, and the nozzle traversal speed was 50 mm/s. The movement of the nozzle followed a zig-zag pattern. The morphology and dimensions of the deposits are given in Fig. S1 (seen supplementary information). After spraying, the substrate was removed and a layer of the deposit with a thickness of more than 2 mm was extracted by electrical wire cutting for further analysis.

2.3 Sintering process

The melting point of CoCrNi MEA powder was confirmed by a differential scanning calorimeter (DSC, Netzsch, STA449F3), from room temperature to 1450 °C, under a heating rate of 10 °C/min in a flowing argon atmosphere, as shown in Fig. 3 (a). As there was no obvious dimensional shrinkage during sintering as-fabricated CSAM deposit, the shrinkage behavior of cold pressed MEA sample was also analyzed by dilatometer (DIL, 402C, Netzsch) to identify proper sintering temperatures of CoCrNi alloy. For the as-fabricated sample, no obvious shrinkage behavior was found during sintering as the temperature was increased to 1350 °C (Fig. 3 (b), blue line), showing a superior dimension accuracy after sintering the as-deposited specimens. However, a starting temperature of shrinkage was identified at approximately 1160 °C for the cold-pressed samples, which means that sintering could be activated at a temperature higher than 1160 °C. In general, the effect of the sintering time on the densification is not as great as that of sintering temperature [33]. This is because the density of sintered sample changes rapidly with holding time in the initial sintering stage. If only prolonging sintering time, which can reduce the productivity, it is difficult to achieve fully dense samples. Therefore, increasing the sintering temperature as much as possible adopted to ensure product performance. Based on these measurements, different sintering strategies were designed and applied to the as-fabricated deposits. The deposits were sintered at the temperatures of 1200 °C, 1250 °C, 1300 °C and 1350 °C for 30 mins in an argon environment in a tube furnace with a heating rate of 10 °C /min, followed by

furnace cooling. After sintering, the densities of the sintered deposits were determined by a density balance (Sartorius SQP).

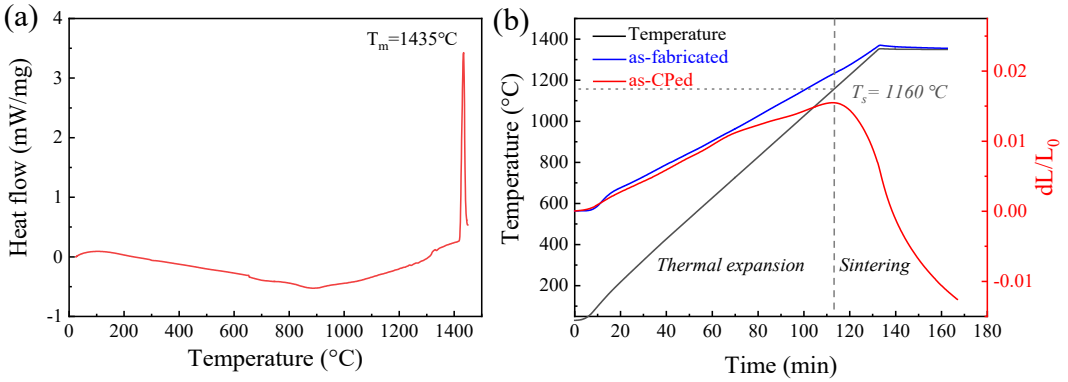

Fig. 3 (a) DSC curve of CoCrNi MEA powder shows the melting point (T_m) and (b) DIL curves of sintered CSAM (blue line) and cold-pressed samples (red line)

2.4 Materials characterization

The as-fabricated and sintered samples were sectioned by electrical wire cutting for microstructure characterization. The samples were prepared by grinding on fine sandpaper and then polishing. And stress-free surfaces for the EBSD experiment were produced by fine polishing with oxides particle solution (OPS, SiO_2, 50nm). The synchronous acquirement of EBSD and EDS signal was achieved in a SEM system (Merlin, Zeiss). For investigating the microstructure at sub-micron level, the polished samples were also characterized through electron channel contrast imaging (ECCI, Sigma 300, Zeiss) and transmission electron microscopy (TEM, Talos F200X, FEI). The TEM specimens were prepared by different procedures: for the as-fabricated sample, a focused ion beam system (FIB, Helios G4, FEI) was used for sampling TEM specimen until the thickness was under 100 nm; for the sintered and deformed samples

(sampling from the 1350 ℃ sintered deposits), the 3mm diameter discs were ground down to 30 μm and then polished via a precision ion polishing system (Gatan 695).

2.5 Mechanical tests

The hardness experiment was conducted on the deposits as well as the sintered samples by using a Vickers hardness tester (HV-1000Z) under a load of 2 N. Fig. 4 shows the dimensions of the tensile samples prepared by electrical wire cutting. Room temperature tensile testing was performed on a universal testing machine (TestStar, Wance) with a laser extensometer at a strain rate of 10^{-3}/s. The average mechanical properties from the three samples, from the as-fabricated and 1350 °C sintered samples, were used in this study. After tensile testing, the fracture surfaces were characterized by SEM (Merlin, Zeiss). In addition, EBSD (Digview 4, EDAX) and TEM (Talos F200X, FEI) analysis were conducted on the deformed sample in the vicinity of the fracture surfaces to investigate the deformation mechanism of the 1350 ℃ sintered CoCrNi sample. Pre-stretching tests on the 1350 °C sintered samples were undertaken and terminated at the strain levels of 5%, 20%, respectively. ECCI was also applied to study the deformation mechanism of the 1350 ℃ sintered CoCrNi samples.

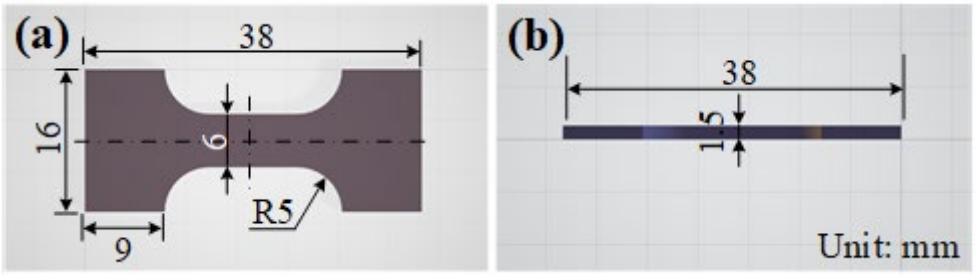

Fig. 4 Geometric dimensions of the tensile sample in (a) top view and (b) left side view

3. Experimental results

3.1 Microstructures

Fig. 5 (a-c) illustrate the cross-sectional EBSD IPF, Kernel Average Misorientation (KAM) and corresponding EDS maps of the as-fabricated CoCrNi MEA samples. As compared to the grain structure of the initial powders (Fig. 2 (c)), the grains of the deformed particles showed a typical bimodal distribution with coarse grains in the center surrounded by refined nanograins. The refined nanograins were resulted from dynamic recrystallization at the highly deformed regions near the interparticle interfaces [34]. The plastic deformation levels in the local area of the as-fabricated specimens were revealed by the KAM map in Fig. 5 (b). Typically, a higher KAM indicates a larger deformation and a higher dislocation density [35]. As such, the local area near the interparticle interfaces was of higher plastic deformation as compared to the interiors of the deformed particles. The EDS maps shown in Fig. 5 (c) indicate that there was no segregation of alloying elements in the deposit after CSAM.

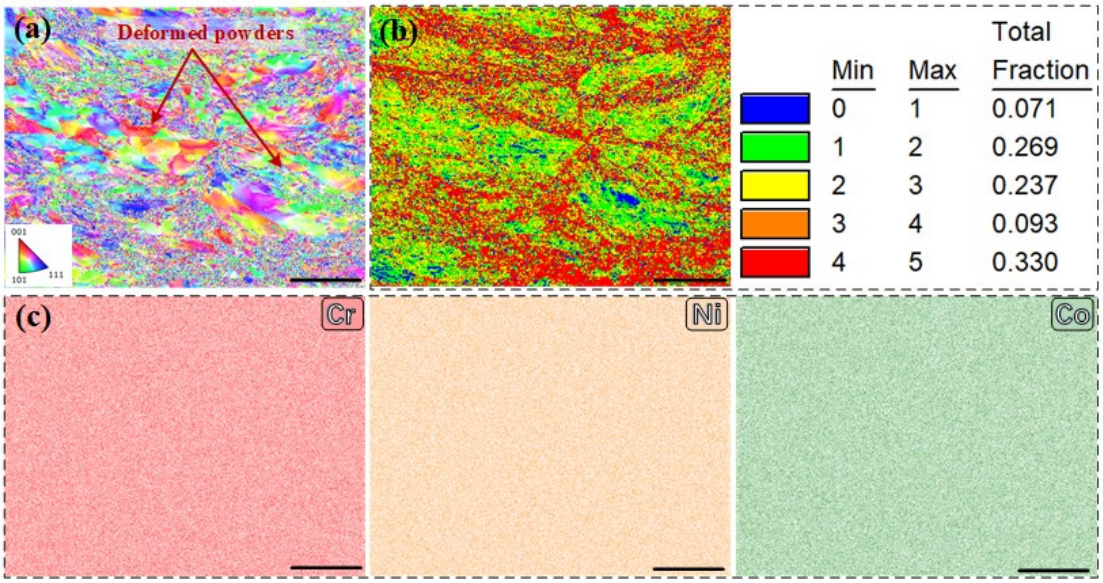

Fig. 5 EBSD results on the as-fabricated CSAM sample. (a) IPF map, (b) KAM map with corresponding misorientation counts, and (c) EDS maps (scale bar is 20 μm)

Fig. 6 shows the cross-sectional EBSD IPF, image quality (IQ) and EDS maps of the sintered deposits at different sintering temperatures. When the sintering temperatures were 1200 °C and 1250 °C, as shown in Fig. 6 (a) and (b), the recrystallization process was incomplete with some fine-grain regions remaining in the deposits, as marked by red-dash circles. Irregular interparticle pores were also found in the deposits. By increasing the sintering temperature to 1300 °C, the fine-grain zones were completely eliminated through recrystallization, and a transformation of the irregular pores to spherical pores was triggered (Fig. 6 (c)). In addition, the pores were mainly located at grain boundaries. However, the incomplete sintered powders were still recognized at the area indicated by the black arrow, where sintering necks were found between the two grains with different orientations. The ECCI image of the 1200 °C sintered sample can also support the formation of sintering necks, given in Fig.

S2 (seen supplementary information). As the sintering temperature was further increased to 1350 °C, the grain size increased significantly to well exceed the median size of the powders (Fig. 7 (b)), indicating a nearly full transformation from sintering necks (between adjacent powders) to grain boundaries. Pores were formed not only at the grain boundaries but also in the grains (Fig. 6 (d)), which indicate the final sintering stage. Hence, 1350 °C was shown to be the optimal temperature condition for sintering the CoCrNi deposits in this study. Moreover, the EDS map shown in Fig. 6 demonstrates that no segregation of Cr occurred after sintering. For quantitatively revealing the difference in grain structure among the starting powders, the as-fabricated samples and the sintered samples, Fig. 7 and Table 1 show the comparison among the powders, the as-fabricated, and the sintered samples in terms of grain size distributions and average grain size. Clearly, the CSAM process resulted in a grain refinement due to severe plastic deformation, while the sintering process caused a significant grain growth through recrystallization, and a higher sintering temperature led to larger grains.

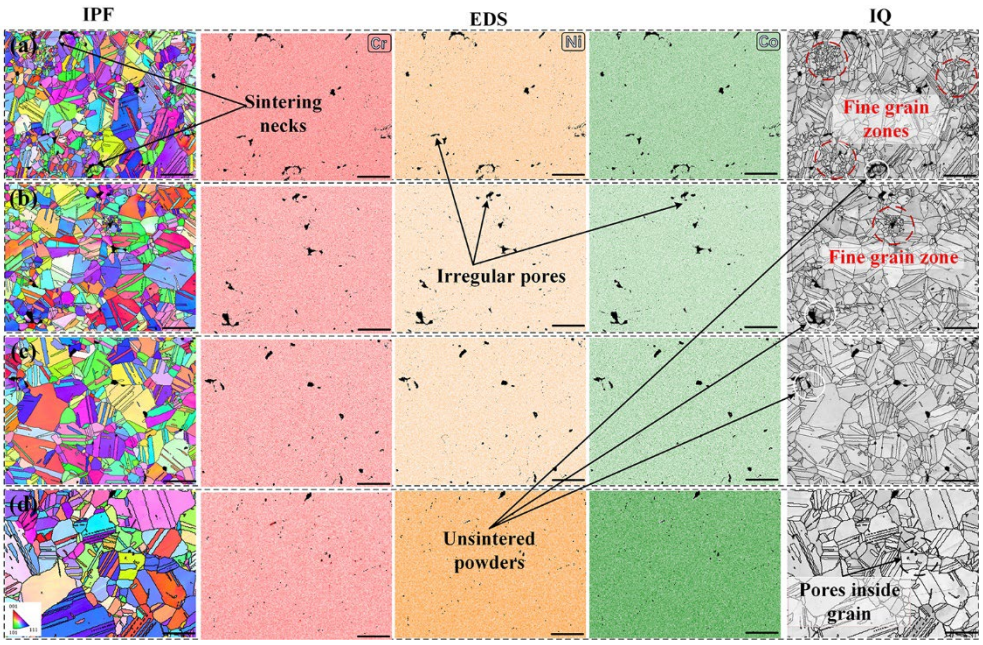

Fig. 6 The IPF maps (first column), the corresponding element EDS maps as well as IQ maps (last maps) of CSAM samples sintered at (a) 1200 °C, (b) 1250 °C, (c) 1300 °C and (d) 1350 °C for 30 min (scale bar is 50 μm)

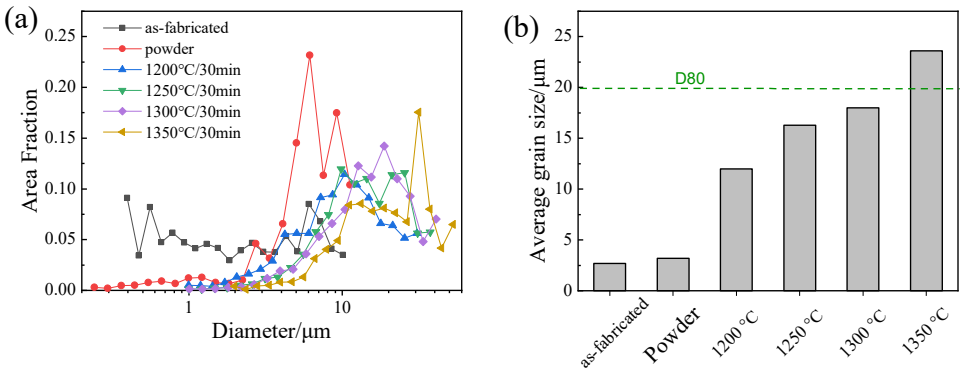

Fig. 7 Grain structure information of the starting powders, as-fabricated samples and sintered samples. (a) grain size distribution and (b) average grain size

Table 1 Basic properties of the starting powders, as-fabricated samples and sintered samples.

Sample status	Powder	CSAM	1200 °C /30min	1250 °C/ 30min	1300 °C /30min	1350 °C /30min

Density (g/cm^3)	-	7.78±0.02	7.79±0.03	7.78±0.03	7.82±0.03	7.82±0.02
Grain size (μm)	3.2	2.7	12	16.3	18	23.6
Hardness (HV)	166.3±5.2	375.8±1.9	239.3±0.9	211.1±1.6	172.7±2.4	169.4±4.3

The as-fabricated and the 1350 °C sintered samples were further studied by ECCI and TEM, and the results are shown in Fig. 8. Deformed grains and interparticle pores were found in the as-fabricated sample (Fig. 8 (a)). The TEM image with the inserted selected area electron diffraction (SAED) pattern and the corresponding EDS maps of the as-fabricated sample indicate that ultra-fine grains were formed in the deposit. After sintering, recrystallization was activated, resulting in grain growth and the formation of sintering twins as illustrated in Fig. 8 (b). Furthermore, from the TEM results shown in Fig. 8 (c, d), it is found that no elemental segregation occurred after CSAM and even after sintering.

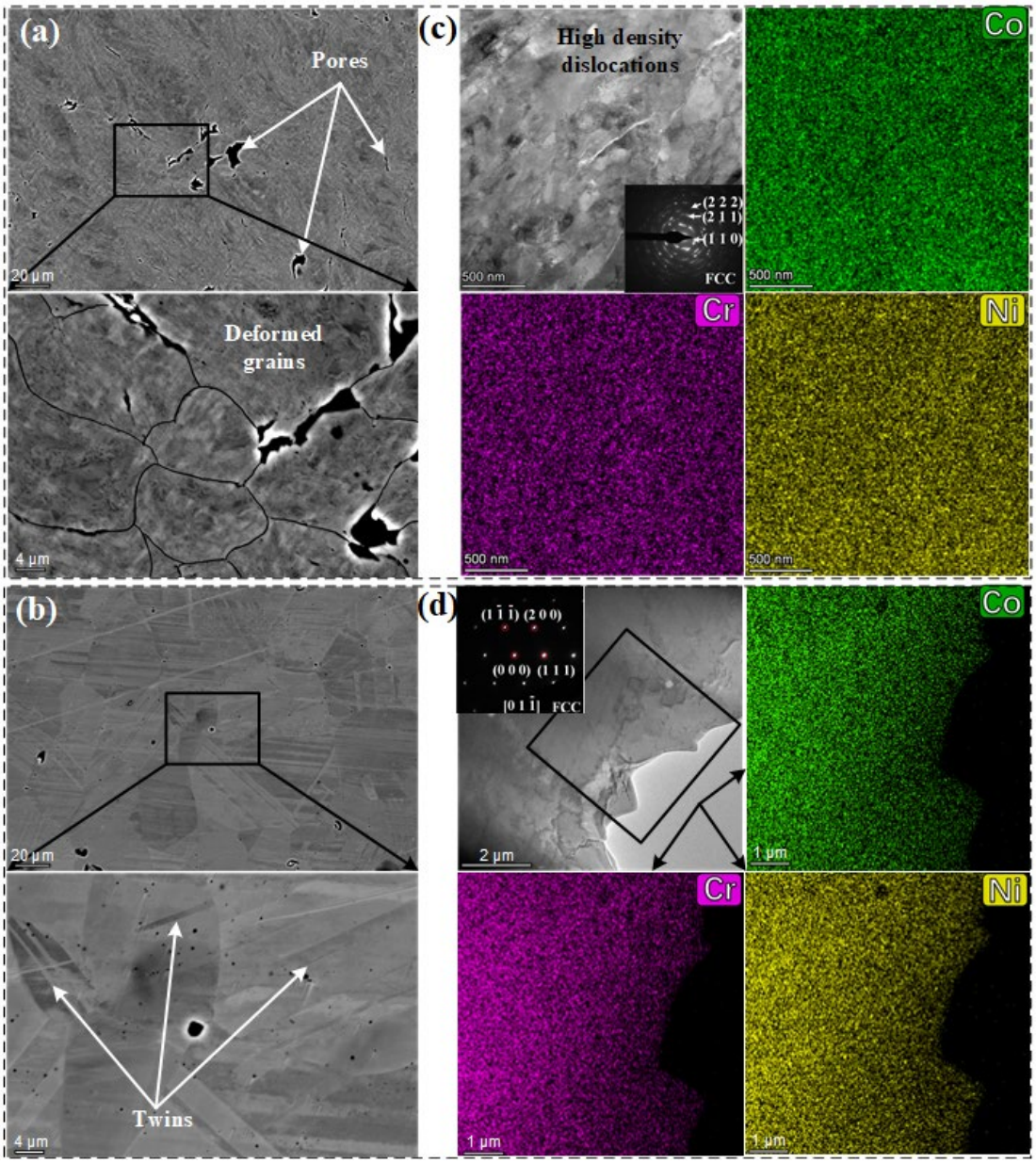

Fig. 8 ECCI and TEM images of the as-fabricated and the 1350 °C sintered samples: (a) ECCI image of the as-fabricated sample, (b) ECCI image of the sintered sample, (c) TEM images and the corresponding EDS maps of the as-fabricated sample, (d) TEM images and the corresponding EDS maps of the sintered sample. The SAED patterns in (c) and (d) show ultra-fine polycrystalline with FCC structure in the as-fabricated sample and large FCC grains in the sintered sample (z=[0 1 1])

3.2 Mechanical properties

The hardness measurements were conducted on the as-received powder, the deposit as well as the sintered samples, which results are listed in Table 1 with the indentation morphologies given in Fig. S3 (seen Supplementary information). As the powder was fabricated via the gas atomization process, the as-received MEA powder has a relatively low Vickers hardness of 166.3 HV, while the hardness of deposit (375.8 HV) was more than twice of that in powder due to the highly deformed structure in the deposit. After sintering at low temperatures (1200 and 1250 °C), the hardness of the as-sintered samples was down to 239.3 and 211.1 HV, respectively, which is slightly higher than the as-received powder. This is because that the incomplete recrystallization process after sintering at those temperatures. By increasing the sintering temperatures, the hardness of sintered samples was stabilized at ~170 HV, similar to that of the as-received powder.

Room temperature tensile test was performed on the as-fabricated as well as the sintered samples. Fig. 9 (a) shows the tensile strain-stress curves of the as-fabricated sample and the 1350 °C sintered sample. As can be seen, the as-fabricated sample was rather brittle; the ultimate tensile strength (UTS) and elongation were ~220 MPa and ~2%, respectively. After sintering treatment, both the UTS and elongation significantly increased to ~660 MPa and ~43% respectively, indicating a synchronous improvement of strength and ductility after sintering. Fig. 9 (b) shows the work hardening rate as a function of true strain for the sintered sample. Based on the true strain-hardening rate

curve, the plastic deformation process of the sample can be divided into three stages. In stage I, a high strain-hardening rate with a dramatic decrease was identified until the strain reached ~ 5% [36]. After that, the strain-hardening rate remained at a constant value of ~1500 MPa until reaching a true strain of 34%. In the last stage, a sudden decrease was observed, indicating the occurrence of fracture.

Fig. 9 (c) compares the UTS and the fracture strain of the sintered sample fabricated in this study and other samples reported in the literature prepared by other techniques including spark plasma sintering (SPS) [37–40], selective laser melting (SLM) [41], laser aided additive manufacturing (LAAM) [42] and direct energy deposition (DED) [43]. As can be seen, the UTS of the sintered sample was not comparable to most of the other MEAs, but the fracture strain of the sintered sample was the second-highest among these MEAs.

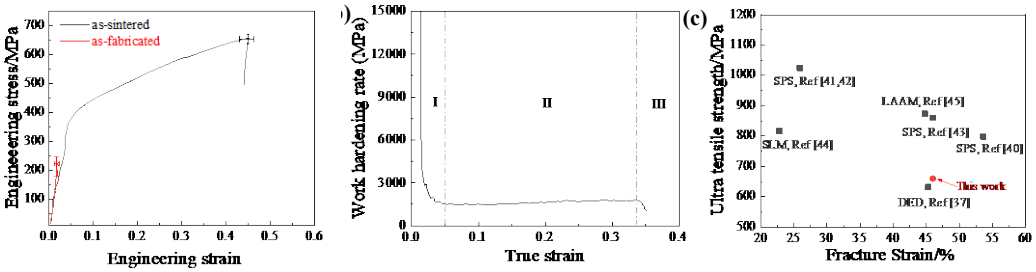

Fig. 9 Mechanical properties of the as-fabricated and 1350 ℃ sintered sample: (a) typical engineering strain-stress curves of the as-fabricated and sintered samples; (b) work hardening rate-true strain curves of the 1350 °C sintered sample, and (c) comparison of the UTS and fracture strain between the sintered sample fabricated in this study and the CoCrNi MEAs made by other PM [37–40] and AM techniques [41–43].

Fig. 10 shows the fracture surface of the as-fabricated and the 1350 ℃ sintered samples after tensile test. For the as-fabricated sample shown in Fig. 10 (a), the fracture surface was characterized by intergranular-like features with few dimples, and the fracture mainly occurred at the interparticle interfaces. This indicates that the interparticle bonding was dominated by mechanical interlocking and physical bonding [44]. After sintering (Fig. 10 (b)), dimple-like features were rather prominent, and it is hard to see any interparticle interfaces, which suggests a significant improvement of ductility.

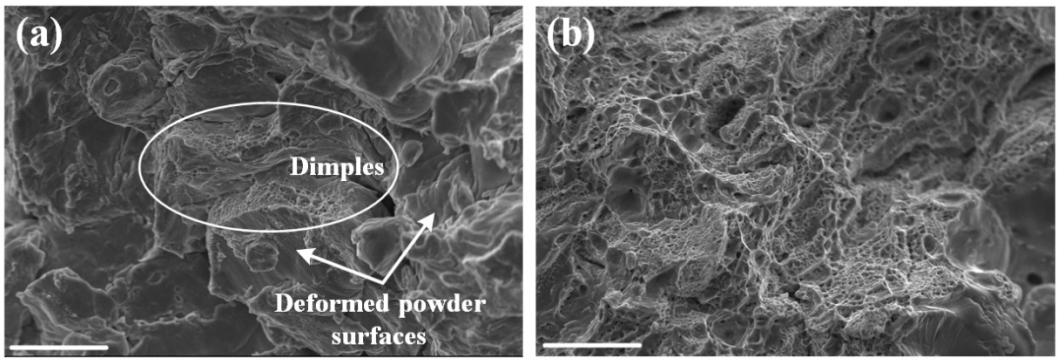

Fig. 10 Fracture morphologies of (a) the as-fabricated sample and (b) the1350 ℃ sintered sample (scale bar is 20 μm)

3.3 Deformation behaviors in sintered deposits

After sintering, there were no obvious fibber texture observed on the sintered samples (supported by Fig. S4 in supplementary information), which renders these samples suitable for the investigation of deformation mechanisms. The deformed microstructure of the 1350 °C sintered deposits was characterized by EBSD, ECCI and TEM in the region next to the fracture, as shown in Fig. 11. Fig. 11 (a) illustrates that the deformation twins were formed after dramatic deformation, whereas no phase

transformation was observed in Fig. 11 (b) indicating that hexagonal close-packed (HCP) phase was observed in the deformed area. In general, the content of HCP phase after deformation would increase when the deformation occurred at a low temperature [45]. However, during room temperature deformation, only a little HCP phase with several atomic layer thicknesses next to twin boundaries [46,47] can be formed. This is why HCP phase was not detected in the deformed CoCrNi sample by EBSD. The TEM map of the deformed area as shown in Fig. 11 (c) also reveals the presence of deformation twins, which is further supported by the SAED pattern detected in the same area.

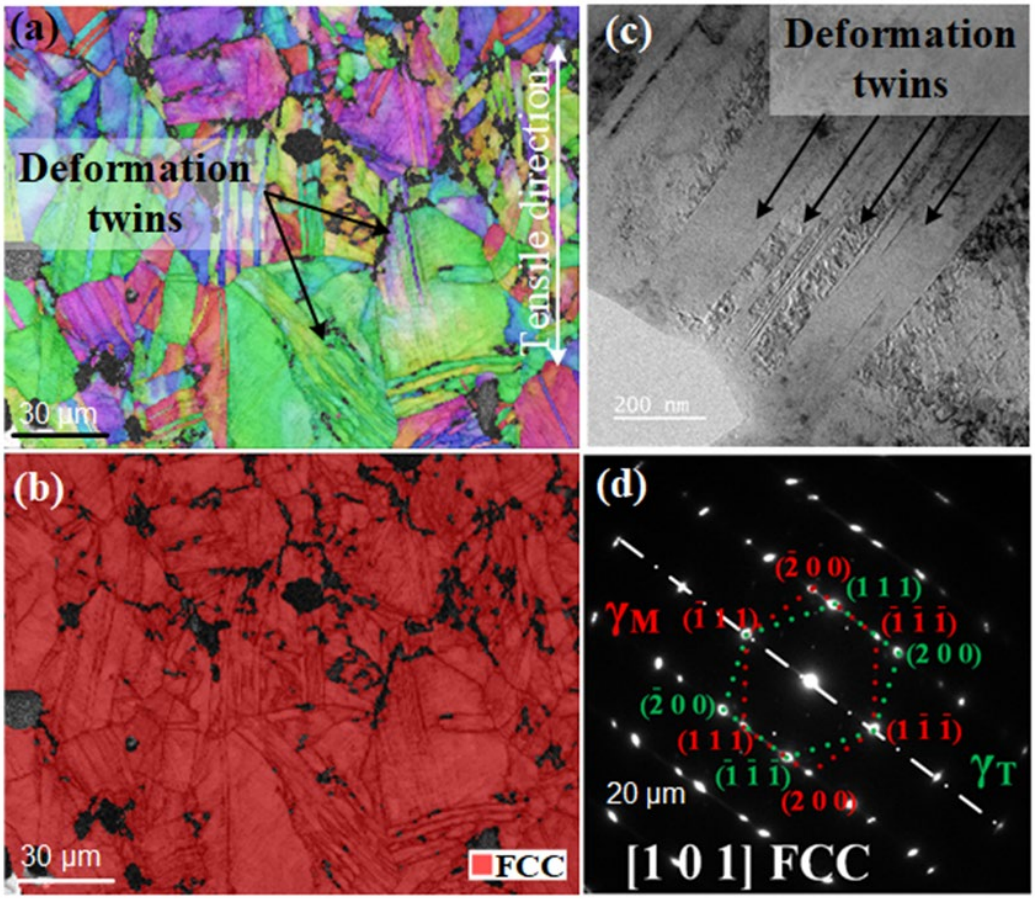

Fig. 11 Deformed microstructure next to the fracture surface of the 1350 ℃ sintered sample. (a) EBSD IPF map, (b) EBSD phase map, (c) TEM image showing the formation of deformation twins, and (d) SAED pattern showing the formation of deformation twins (Z = [1 0 1])

To further reveal the deformation mechanism of the sintered sample, Fig. 12 shows the ECCI images of the 1350 °C sintered sample at the local strain of 0, 5%, 20% and ~45% (with the highest fracture strain) during the pre-tensile test. Before the sample was subject to tensile deformation, twins that were formed during the sintering process were observed in Fig. 12 (a) due to a relatively low stacking fault energy [9]. The sintering process caused the occurrence of recrystallization which resulted in the growth of grains through the migration of grain boundaries [48]. During grain growing, when

a layer of atoms was hindered at grain boundaries corner, stacking sequences were changed to form a twin boundary [49]. For the deformed samples, as can be seen in Fig. 9 (b), the deformation of can be divided into three different stages. The ECCI images in Fig. 12 (b, c, d) show the microstructure of the deformed sample at the end of stage I (ε_{loc}=0.05), stage II (ε_{loc}=0.2) and stage III ($\varepsilon_{loc}\approx$0.45), respectively. From Fig. 12 (b), only a system of slip planes, represented by the bright broken lines [47], were observed in the grain. As the local strain was increased to 0.2, bright lines were visible as shown Fig. 12 (c), which indicates the formation of deformation twins at this stage [47]. At this strain level, deformation twins played an important role in deforming CoCrNi MEA [38,45–47]. At the final stage ($\varepsilon_{loc}\approx$0.45), rupture took place after the deformation twins were heavily formed as shown in Fig. 12 (d).

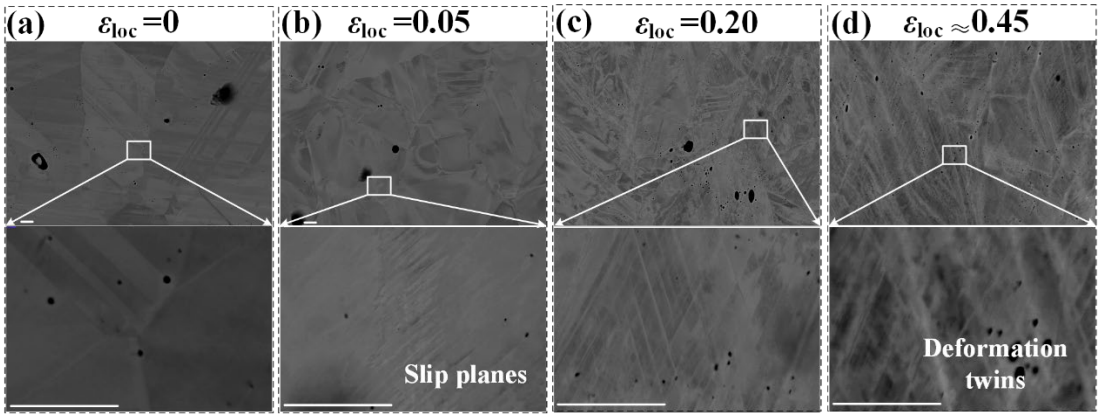

Fig. 12 ECCI images of the 1350 °C sintered deposits at the local strain of (a) 0, (b) 5%, (c) 20% and (d) ~45% during the pre-tensile test (scale bar is 5 μm)

4. Discussion

4.1 Sintering mechanism on CSAM deposits

For HEAs and MEAs, the sintering temperature would be increased to a high level due to the sluggish diffusion effects [50], as proven in a previous study [51]. The DSC curve shown in Fig. 3 (a) confirms that no phase transformation occurred during the sintering process under the applied sintering temperature (i.e., 1200 °C – 1350 °C). In sintering process, the deformation energy generated during the CSAM process provides a driving force for recrystallization in the first stage, which is similar to the sintering of cold-pressed green samples [17,25,30,52]. Recrystallization, sintering necks and polycrystalline growth occur consecutively [32]. The DIL curve of the cold-pressed sample in Fig. 3 (b) (red line) gives the starting sintering temperature of CoCrNi MEA of ~ 1160 °C, meaning that a sintering temperature higher than that temperature would promote the dramatic atomic diffusion as well as the formation and growth of sintering necks formed between adjacent particles. The whole sintering process can be summarized as follows:

Fine grains were formed (Fig. 6 (a-b)) due to the incomplete recrystallization by inadequate sintering temperature，when the temperatures were lower than 1300 °C. Under these low sintering temperatures, interparticle boundaries as seen in Fig. 8 (a) could be eliminated and replaced by neck formation (Fig. 6). On the other hand, irregular openings were found in the sample, as can be seen in Fig. 6 (a-b), which indicates the initial stage of the sintering process [53]. With the sintering temperature

increased to 1300 °C, the transformation of pores from irregular to spherical shape was promoted. At this intermediate sintering, the merge of adjacent necks and atomic diffusion were promoted. However, the characteristics of incompletely sintered powders, as seen in Fig. 6 (c), indicate an unfinished migration of sintering necks between adjacent powders at a sintering temperature of 1300 °C. By further increasing the sintering temperature to 1350 °C, the isolated spherical shape pores (shown in Fig. 6 (d)) were transformed from irregular openings, which was activated by the migration of vacancies around these openings [54]. At the final stage of sintering, the growth of grains and strengthening of deposits occurred. The transformation of the bonding mechanism from the interparticle mechanical interlocks in as-fabricated specimens to metallurgical bonding in sintered samples was achieved, which led to the synchronous enhancement of strength and ductility.

The interfaces between the particles after CSAM are generally the weak points during deformation [10,55]. When the grains became larger than the particle size, a total transformation from mechanical to metallurgical bonding was achieved. Hence, it is important to unravel the laws of grain growth in the CoCrNi MEA. The grain growth is a function of temperature (Arrhenius law), given as follows [56],

$$G_s = G_0 \cdot \exp[-A/(R \cdot T)] \quad \text{(Eq. 1)}$$

where G_s and G_0 are grain size in the sintered and initial samples, A denotes the activation energy of grain growth, R is the ideal gas constant and T is the sintered temperature (K). Taking the logarithm of Eq. 1, gives the following equation,

$$\ln\left(G_s/G_0\right) = -A/(R \cdot T) \quad \text{(Eq. 2)}$$

By using the grain size listed in Table 1 and the sintering temperatures, the logarithms of (G_s/G_0) versus 1/T were plotted in Fig. 13. In addition, the best fitting line was found in Fig. 13 for the calculation of effective activation energy of grain growth. By calculating the slope of the fitted line, the activation energy for grain growth of CoCrNi MEA was 84.15 kJ/mol, and can be used for predicting the level of grain growth during sintering.

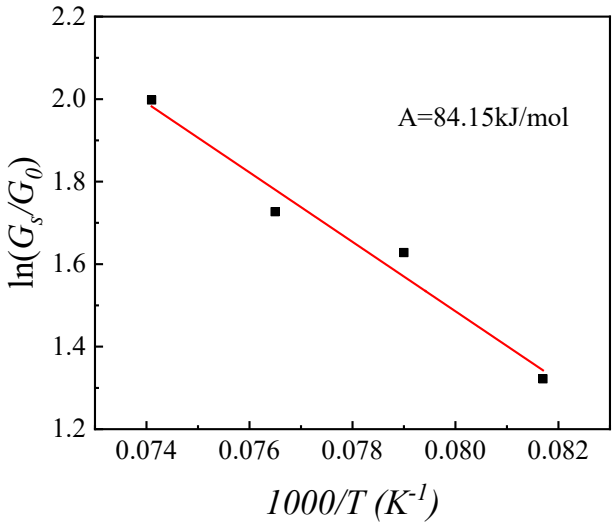

Fig. 13 Logarithm of average grain size versus the inverse of sintering temperature for CoCrNi MEA solid solution

4.2 Enhancement mechanism on mechanical properties of sintered deposits

The as-fabricated CoCrNi deposit showed unfavorable mechanical properties, and this is a common phenomenon that has been frequently seen in CSAM deposits, particularly for high-strength materials [17,25,30]. Extreme compressive stress generated during the supersonic impact of powders can promote local adiabatic shear

instability at an ultra-high strain rate [57]. The extensive plastic deformation of the CoCrNi powders caused by high-speed impact led to the formation of a large number of deformed grains as well as high local strain [58,59] (Fig. 5). On the fracture surface of the tensile sample, very few dimple-like features could be observed for the as-fabricated sample, which implies limited metallurgical bonding formed. When the powders were deposited on the previous layer, energy transformation from kinetic energy to thermal energy occurred [13]. Such transformation could lead to the localized temperature at the highly deformed interfacial region reaching a temperature close to the material melting temperature [60]. However, the area of such high-temperature interfaces was very limited which led to interparticle fracture and the poor mechanical properties given in Fig. 9 (a).

Annealing has been proven to be an effective method to strengthen and toughen as-fabricated deposits [17,19,20,25–31]. It improves the mechanical properties mainly through inducing recovery and recrystallization, and partially promotes the atomic diffusion between adjacent particles at the same time [17]. However, as the annealing temperature is normally set at a level of 0.4 to 0.5 of melting temperature [61], the migration of grain boundaries through the interface of adjacent particles cannot be greatly activated [32]. Therefore, sintering which requires a processing temperature of 0.7 to 0.8 of the melting temperature has been applied to induce the migration of the grain boundaries and to significantly improve the mechanical properties of conventional alloys [32]. Different from the limited metallurgical bonding between

adjacent particles after the annealing, sintering resulted in the extension of sintering neck and grain growth. By increasing the sintering temperature to 1350 °C, grain boundaries can migrate across pores resulting in the annihilation of pores (Fig. 8) and an increase of strength in sintered deposits as shown in Fig. 9 (a), and a ductile fracture mode was identified in sintered specimens (Fig. 10 (b)).

5. Conclusions

A combined CSAM-sintering strategy was applied to fabricate high-performance CoCrNi MEA deposits. Samples were firstly fabricated via CSAM using nitrogen as propulsive gas at 5.0 MPa and 1000 °C, and the as-fabricated samples were then subject to sintering at different temperatures. Based on the experimental results, the microstructures, mechanical properties and tensile deformation mechanisms of the samples were discussed, and the conclusions of the study are as follows:

1) CSAM is capable of fabricating dense CoCrNi MEA deposits. After the CSAM process, interparticle boundaries could be found along the fracture surface of the as-fabricated sample, indicating the weak bonding between adjacent particles. Due to the high strain rate deformation of the CoCrNi particles during CSAM, grains severely deformed, which provides a driving force for the recovery and recrystallization during the following sintering process.
2) The CSAM samples sintered at different temperatures were characterized by different microscopic techniques. At lower sintering temperatures (1200 °C and 1250 °C), incomplete recrystallization processes were identified, while irregular

pores were found on the grain boundaries of the sample sintered at 1300 °C, which indicates imperfect sintering. By increasing the sintering temperature to 1350 °C, the microstructure and intragranular pores reflect the characteristics of the last sintering stage, indicating a complete sintering process.

3) Room temperature tensile tests reveal that sintering treatment significantly improved the UTS and elongation from 220 MPa and 2% respectively for the as-fabricated sample to ~660 MPa and ~ 43% for the 1350 °C sintered sample.

4) The deformation mechanism of the 1350 °C sintered deposits was studied. Under a low local strain level (5%), slip planes were triggered in grains. Increasing the strain level resulted in the formation of deformation twins and a high working hardening rate.

Acknowledgements

The work described in this paper was mainly supported by the funding support to the State Key Laboratories in Hong Kong from the Innovation and Technology Commission (ITC) of the Government of the Hong Kong Special Administrative Region (HKSAR), China. The authors would also like to express their sincere thanks to the financial support from the Research Committee of The Hong Kong Polytechnic University through the research student project (account code: RK3K), the National Natural Science Foundation of China (Grant No. 52104362), the Shenzhen Science and Technology Innovation Committee (Grant No. KQJSCX20180322152424539), the Research Fund of the State Key Laboratory of Solidification Processing (Grant No.

SKLSP202011), the International Cooperation Project of Guangdong Province (Grant No. 2021A0505030052) and the Guangdong Major Project of Basic and Applied Basic Research, China (Grant No. 2019B030302010).

References

[1] Yeh J, Chen S, Lin S, Gan J, Chin T, Shun T, et al. Nanostructured High-Entropy Alloys with Multiple Principal Elements : Novel Alloy Design Concepts and Outcomes. Adv Eng Mater 2004;6:299–303. https://doi.org/10.1002/adem.200300567.

[2] Lei Z, Liu X, Wu Y, Wang H, Jiang S, Wang S, et al. Enhanced strength and ductility in a high-entropy alloy via ordered oxygen complexes. Nature 2018;563:546–50. https://doi.org/10.1038/s41586-018-0685-y.

[3] Lei Z, Wu Y, He J, Liu X, Wang H, Jiang S, et al. Snoek-type damping performance in strong and ductile high-entropy alloys. Sci Adv 2020;6:1–9. https://doi.org/10.1126/sciadv.aba7802.

[4] Yin S, Li W, Song B, Yan X, Kuang M, Xu Y, et al. Deposition of FeCoNiCrMn high entropy alloy (HEA) coating via cold spraying. J Mater Sci Technol 2019;35:1003–7. https://doi.org/10.1016/j.jmst.2018.12.015.

[5] Kai W, Li CC, Cheng FP, Chu KP, Huang RT, Tsay LW, et al. The oxidation behavior of an equimolar FeCoNiCrMn high-entropy alloy at 950 ◦ C in various oxygen-containing atmospheres. Corros Sci 2016;108:209–14. https://doi.org/10.1016/j.corsci.2016.03.020.

[6] Xu Y, Li W, Qu L, Yang X, Song B, Lupoi R, et al. Solid-state cold spraying of FeCoCrNiMn high-entropy alloy: an insight into microstructure evolution and oxidation behavior at 700-900 °C. J Mater Sci Technol 2021;68:172–83. https://doi.org/10.1016/j.jmst.2020.06.041.

[7] He H, Naeem M, Zhang F, Zhao Y, Harjo S, Kawasaki T, et al. Stacking Fault Driven Phase Transformation in CrCoNi Medium Entropy Alloy. Nano Lett 2021;21:1419–26. https://doi.org/10.1021/acs.nanolett.0c04244.

[8] Gludovatz B, Hohenwarter A, Thurston KVS, Bei H, Wu Z, George EP, et al. Exceptional damage-tolerance of a medium-entropy alloy CrCoNi at cryogenic temperatures. Nat Commun 2016;7:1–8. https://doi.org/10.1038/ncomms10602.

[9] Zhang R, Zhao S, Ding J, Chong Y, Jia T, Ophus C, et al. Short-range order and its impact on the CrCoNi medium-entropy alloy. Nature 2020;581:283–7. https://doi.org/10.1038/s41586-020-2275-z.

[10] Yin S, Cavaliere P, Aldwell B, Jenkins R, Liao HL, Li WY, et al. Cold spray additive manufacturing and repair: Fundamentals and applications. Addit Manuf 2018;21:628–50. https://doi.org/10.1016/j.addma.2018.04.017.

[11] Li W, Yang K, Yin S, Yang X, Xu Y, Lupoi R. Solid-state additive manufacturing and repairing by cold spraying: A review. J Mater Sci Technol 2018;34:440–57. https://doi.org/10.1016/j.jmst.2017.09.015.

[12] Li W, Cao C, Yin S. Solid-state cold spraying of Ti and its alloys: A literature review. Prog Mater Sci 2020;110:100633. https://doi.org/10.1016/j.pmatsci.2019.100633.

[13] Wu J, Fang H, Yoon S, Kim H, Lee C. The rebound phenomenon in kinetic spraying deposition. Scr Mater 2006;54:665–9. https://doi.org/10.1016/j.scriptamat.2005.10.028.

[14] Yin S, Cizek J, Cupera J, Hassani M, Luo X, Jenkins R, et al. Formation conditions of vortex-like intermixing interfaces in cold spray. Mater Des 2020;200:109444. https://doi.org/10.1016/j.matdes.2020.109444.

[15] Raoelison RN, Xie Y, Sapanathan T, Planche MP, Kromer R, Costil S, et al. Cold gas dynamic spray technology: A comprehensive review of processing conditions for various technological developments till to date. Addit Manuf 2018;19:134–59. https://doi.org/https://doi.org/10.1016/j.addma.2017.07.001.

[16] Xie X, Yin S, Raoelison R nirina, Chen C, Verdy C, Li W, et al. Al matrix composites fabricated by solid-state cold spray deposition: A critical review. J Mater Sci Technol 2021;86:20–55. https://doi.org/10.1016/j.jmst.2021.01.026.

[17] Yin S, Cizek J, Yan X, Lupoi R. Annealing strategies for enhancing mechanical properties of additively manufactured 316L stainless steel deposited by cold spray. Surf Coatings Technol 2019;370:353–61. https://doi.org/10.1016/j.surfcoat.2019.04.012.

[18] Chen C, Xie Y, Yan X, Yin S, Fukanuma H, Huang R, et al. Effect of hot isostatic pressing (HIP) on microstructure and mechanical properties of Ti6Al4V alloy fabricated by cold spray additive manufacturing. Addit Manuf 2019;27:595–605. https://doi.org/10.1016/j.addma.2019.03.028.

[19] Zhao Z, Tariq N ul H, Tang J, Jia C, Qiu X, Ren Y, et al. Microstructural evolutions and mechanical characteristics of Ti/steel clad plates fabricated through

cold spray additive manufacturing followed by hot-rolling and annealing. Mater Des 2020;185:108249. https://doi.org/10.1016/j.matdes.2019.108249.

[20] Qiu X, Tariq N ul H, Qi L, Zan Y ning, Wang Y jiang, Wang J qiang, et al. In-situ Sip/A380 alloy nano/micro composite formation through cold spray additive manufacturing and subsequent hot rolling treatment: Microstructure and mechanical properties. J Alloys Compd 2019;780:597–606. https://doi.org/10.1016/j.jallcom.2018.11.399.

[21] Zhao Z, Tariq N ul H, Tang J, Ren Y, Liu H, Tong M, et al. Influence of annealing on the microstructure and mechanical properties of Ti/steel clad plates fabricated via cold spray additive manufacturing and hot-rolling. Mater Sci Eng A 2020;775:138968. https://doi.org/10.1016/j.msea.2020.138968.

[22] Zhao Z, Tang J, Tariq N ul H, Liu H, Liu H, Ren Y, et al. Effect of rolling temperature on microstructure and mechanical properties of Ti/steel clad plates fabricated by cold spraying and hot-rolling. Mater Sci Eng A 2020;795:139982. https://doi.org/10.1016/j.msea.2020.139982.

[23] Xie X, Chen C, Chen Z, Wang W, Yin S, Ji G, et al. Achieving simultaneously improved tensile strength and ductility of a nano-TiB2/AlSi10Mg composite produced by cold spray additive manufacturing. Compos Part B Eng 2020;202:108404. https://doi.org/10.1016/j.compositesb.2020.108404.

[24] Petrovskiy P, Sova A, Doubenskaia M, Smurov I. Influence of hot isostatic pressing on structure and properties of titanium cold-spray deposits. Int J Adv Manuf Technol 2019;102:819–27. https://doi.org/10.1007/s00170-018-03233-5.

[25] Li WY, Zhang C, Liao H, Coddet C. Effect of heat treatment on microstructure and mechanical properties of cold sprayed Ti coatings with relatively large powder particles. J Coatings Technol Res 2009;6:401–6. https://doi.org/10.1007/s11998-008-9133-5.

[26] Zahiri SH, Fraser D, Jahedi M. Recrystallization of cold spray-fabricated CP titanium structures. J Therm Spray Technol 2009;18:16–22. https://doi.org/10.1007/s11666-008-9212-2.

[27] Eason PD, Fewkes JA, Kennett SC, Eden TJ, Tello K, Kaufman MJ, et al. On the characterization of bulk copper produced by cold gas dynamic spray processing in as fabricated and annealed conditions. Mater Sci Eng A 2011;528:8174–8. https://doi.org/10.1016/j.msea.2011.07.012.

[28] Hall AC, Cook DJ, Neiser RA, Roemer TJ, Hirschfeld DA. The effect of a simple annealing heat treatment on the mechanical properties of cold-sprayed aluminum. J Therm Spray Technol 2006;15:233–8. https://doi.org/10.1361/105996306X108138.

[29] Tariq NH, Gyansah L, Qiu X, Du H, Wang JQ, Feng B, et al. Thermo-mechanical post-treatment: A strategic approach to improve microstructure and

mechanical properties of cold spray additively manufactured composites. Mater Des 2018;156:287–99. https://doi.org/10.1016/j.matdes.2018.06.062.

[30] Yin S, Jenkins R, Yan X, Lupoi R. Microstructure and mechanical anisotropy of additively manufactured cold spray copper deposits. Mater Sci Eng A 2018;734:67–76. https://doi.org/10.1016/j.msea.2018.07.096.

[31] Fan N, Cizek J, Huang C, Xie X, Chlup Z, Jenkins R, et al. A new strategy for strengthening additively manufactured cold spray deposits through in-process densification. Addit Manuf 2020;36:101626. https://doi.org/10.1016/j.addma.2020.101626.

[32] Upadhyaya GS. Powder metallurgy technology. Cambridge Int Science Publishing; 1997.

[33] Kang S-JL. Sintering: densification, grain growth and microstructure. Elsevier; 2004.

[34] Yin S, Chen C, Suo X, Lupoi R. Cold-Sprayed Metal Coatings with Nanostructure. Adv Mater Sci Eng 2018;2018. https://doi.org/10.1155/2018/2804576.

[35] Gussev MN, Leonard KJ. In situ SEM-EBSD analysis of plastic deformation mechanisms in neutron-irradiated austenitic steel. J Nucl Mater 2019;517:45–56. https://doi.org/10.1016/j.jnucmat.2019.01.034.

[36] Ma Y, Song W, Bleck W. Investigation of the microstructure evolution in a Fe-17Mn-1.5Al-0.3C steel via in situ synchrotron X-ray diffraction during a tensile test. Materials (Basel) 2017;10:1–16. https://doi.org/10.3390/ma10101129.

[37] Wang J, Yang H, Huang H, Ruan J, Ji S. In-situ Mo nanoparticles strengthened CoCrNi medium entropy alloy. J Alloys Compd 2019;798:576–86. https://doi.org/10.1016/j.jallcom.2019.05.208.

[38] Moravcik I, Cizek J, Kovacova Z, Nejezchlebova J, Kitzmantel M, Neubauer E, et al. Mechanical and microstructural characterization of powder metallurgy CoCrNi medium entropy alloy. Mater Sci Eng A 2017;701:370–80. https://doi.org/10.1016/j.msea.2017.06.086.

[39] Wang J, Yang H, Ruan J, Wang Y, Ji S. Microstructure and properties of CoCrNi medium-entropy alloy produced by gas atomization and spark plasma sintering. J Mater Res 2019;34:2126–36. https://doi.org/10.1557/jmr.2019.96.

[40] Huang H, Wang J, Yang H, Ji S, Yu H, Liu Z. Strengthening CoCrNi medium-entropy alloy by tuning lattice defects. Scr Mater 2020;188:216–21. https://doi.org/10.1016/j.scriptamat.2020.07.027.

[41] Niu P, Li R, Gan K, Yuan T, Xie S, Chen C. Microstructure, Properties, and Metallurgical Defects of an Equimolar CoCrNi Medium Entropy Alloy Additively Manufactured by Selective Laser Melting. Metall Mater Trans A Phys Metall Mater Sci 2021;52:753–66. https://doi.org/10.1007/s11661-020-06121-4.

[42] Weng F, Chew Y, Zhu Z, Yao X, Wang L, Ng FL, et al. Excellent combination of strength and ductility of CoCrNi medium entropy alloy fabricated by laser aided additive manufacturing. Addit Manuf 2020;34:101202. https://doi.org/10.1016/j.addma.2020.101202.

[43] Xue P, Zhu L, Ning J, Ren Y, Yang Z, Wang S, et al. Effect of laser incident energy on the densification and structure–property relationships of additively manufactured CrCoNi medium-entropy alloy. Virtual Phys Prototyp 2021;16:404–16. https://doi.org/10.1080/17452759.2021.1947509.

[44] Assadi H, Kreye H, Gärtner F, Klassen T. Cold spraying – A materials perspective. Acta Mater 2016;116:382–407. https://doi.org/10.1016/j.actamat.2016.06.034.

[45] Kim YS, Chae H, Woo W, Kim DK, Lee DH, Harjo S, et al. Multiple deformation scheme in direct energy deposited CoCrNi medium entropy alloy at 210K. Mater Sci Eng A 2021;828:142059. https://doi.org/10.1016/j.msea.2021.142059.

[46] Li J, Li L, Jiang C, Fang Q, Liu F, Liu Y, et al. Probing deformation mechanisms of gradient nanostructured CrCoNi medium entropy alloy. J Mater Sci Technol 2020;57:85–91. https://doi.org/10.1016/j.jmst.2020.03.064.

[47] Slone CE, Chakraborty S, Miao J, George EP, Mills MJ, Niezgoda SR. Influence of deformation induced nanoscale twinning and FCC-HCP transformation on hardening and texture development in medium-entropy CrCoNi alloy. Acta Mater 2018;158:38–52. https://doi.org/10.1016/j.actamat.2018.07.028.

[48] Hu J, Wang X, Zhang J, Luo J, Zhang Z, Shen Z. A general mechanism of grain growth ─I. Theory. J Mater 2021;7:1007–13. https://doi.org/10.1016/j.jmat.2021.02.007.

[49] Ji K sheng, Song G sheng, Song H wu, Zhang S hong. Annealing twin mechanism for 304 stainless steel solution treatment process. J Cent South Univ 2021;28:1978–89. https://doi.org/10.1007/s11771-021-4746-2.

[50] Chen BR, Yeh AC, Yeh JW. Effect of one-step recrystallization on the grain boundary evolution of CoCrFeMnNi high entropy alloy and its subsystems. Sci Rep 2016;6:1–9. https://doi.org/10.1038/srep22306.

[51] Zhang Y, Bian T, Shen X, Wang Z, Ye S, Feng S, et al. Sintering mechanism and microstructure evolution of a CoCrFeNiMn high entropy alloy fabricated by metal injection molding. J Alloys Compd 2021:158711.

[52] Wu J, Fang H, Kim HJ, Lee C. High speed impact behaviors of Al alloy particle onto mild steel substrate during kinetic deposition. Mater Sci Eng A 2006;417:114–9. https://doi.org/10.1016/j.msea.2005.11.011.

[53] Kini MK, Chokshi AH. Initial stage sintering of polycrystalline spheres : A model and experiments. Materialia 2020;10:100665. https://doi.org/10.1016/j.mtla.2020.100665.

[54] Kornyushin Y. Thermodynamic Theory of Sintering and Swelling. Met Noveishie Tekhnol 2007;29:949–70.

[55] Wu H, Xie X, Liu S, Xie S, Huang R, Verdy C, et al. Bonding behavior of Bi-metal-deposits produced by hybrid cold spray additive manufacturing. J Mater Process Technol 2022;299. https://doi.org/10.1016/j.jmatprotec.2021.117375.

[56] Coble RL. Sintering crystalline solids. I. intermediate and final state diffusion models. J Appl Phys 1961;32:787–92. https://doi.org/10.1063/1.1736107.

[57] Zou Y, Qin W, Irissou E, Legoux JG, Yue S, Szpunar JA. Dynamic recrystallization in the particle/particle interfacial region of cold-sprayed nickel coating: Electron backscatter diffraction characterization. Scr Mater 2009;61:899–902. https://doi.org/10.1016/j.scriptamat.2009.07.020.

[58] Baek M-S, Kim H-J, Lee K-A. Anisotropy of Compressive Deformation Behavior in Cold Sprayed Cu Bulk Material. J Nanosci Nanotechnol 2019;19:3935–42. https://doi.org/10.1166/jnn.2019.16147.

[59] Bhattiprolu VS, Johnson KW, Crawford GA. Influence of Powder Microstructure on the Microstructural Evolution of As-Sprayed and Heat Treated Cold-Sprayed Ti-6Al-4V Coatings. J Therm Spray Technol 2019;28:174–88. https://doi.org/10.1007/s11666-018-0812-1.

[60] Pathak S, Saha GC. Development of sustainable cold spray coatings and 3D additive manufacturing components for repair/manufacturing applications: A critical review. Coatings 2017;7. https://doi.org/10.3390/coatings7080122.

[61] Reed-Hill RE, Abbaschian R, Abbaschian R. Physical metallurgy principles. vol. 17. Van Nostrand New York; 1973.